

Geophysical Research Letters®









RESEARCH LETTER

10.1029/2023GL108091

Asymmetric Influences of ENSO Phases on the Predictability of North Pacific Sea Surface Temperature

Key Points:

- El Niño–Southern Oscillation phases asymmetrically impact North Pacific sea surface temperature (SST) predictability: El Niño (5.5 months), La Niña (8.4 months), Neutral (5.9 months)
- Error growth dynamics vary: La Niña displays strong signals with slow growth, El Niño exhibits weak signals and rapid growth
- A positive heating anomaly from La Niña reduces atmospheric noise impact, resulting in a smaller error growth rate of the North Pacific SST

Zhaolu Hou¹ , Jianping Li^{1,2} , Yina Diao¹ , Yazhou Zhang¹, Quanjia Zhong³ , Jie Feng^{4,5} , and Xin Qi¹ 

¹College of Oceanic and Atmospheric Sciences/Frontiers Science Center for Deep Ocean Multispheres and Earth System/Key Laboratory of Physical Oceanography/Academy of the Future Ocean/Innovation Center for Ocean Carbon Neutrality, Ocean University of China, Qingdao, China, ²Laoshan Laboratory, Qingdao, China, ³Department of Ocean Science, Hong Kong University of Science and Technology, Hong Kong, China, ⁴Department of Atmospheric and Oceanic Sciences/Institute of Atmospheric Sciences, Fudan University, Shanghai, China, ⁵Shanghai Key Laboratory of Ocean–Land–Atmosphere Boundary Dynamics and Climate Change, Fudan University, Shanghai, China

Supporting Information:

Supporting Information may be found in the online version of this article.

Correspondence to:

J. Li and Y. Diao,
ljp@ouc.edu.cn;
diaoyin@ouc.edu.cn

Citation:

Hou, Z., Li, J., Diao, Y., Zhang, Y., Zhong, Q., Feng, J., & Qi, X. (2024). Asymmetric influences of ENSO phases on the predictability of North Pacific sea surface temperature. *Geophysical Research Letters*, 51, e2023GL108091. <https://doi.org/10.1029/2023GL108091>

Received 28 DEC 2023

Accepted 21 MAR 2024

Abstract The North Pacific sea surface temperature (SST) has a profound climatic influence. The El Niño–Southern Oscillation (ENSO) significantly impacts the North Pacific SST; however, the influence of the distinct phases of ENSO on SST predictability remains unclear. To overcome the model limitations, this study assessed SST predictability under diverse ENSO phases using reanalysis. The predictability limit of the North Pacific SST under La Niña (8.4 months) is longer than that under Neutral (5.9 months) and El Niño (5.5 months) conditions, which unveils asymmetry. This asymmetry mirrors contemporary multimodal prediction skills. Error growth dynamics reveal La Niña's robust signal strength with a slow error growth rate, in contrast to El Niño's weaker signal and faster error growth. There exhibits intermediate signal strength and elevated error growth in Neutral condition. Physically, predictability signal strength aligns with SST variability, whereas the error growth rate correlates with atmospheric–ocean heating anomalies. La Niña, which induces positive heating anomalies, minimizes the impact of atmospheric noise, resulting in lower error growth. The result is beneficial for improving North Pacific SST predictions.

Plain Language Summary The North Pacific sea surface temperature (SST) significantly impacts global climate, particularly in East Asia and the United States. Accurate prediction of North Pacific SST, which is crucial for seasonal and interannual forecasting, remains a focal point in atmospheric and oceanic research. This study investigates how the El Niño–Southern Oscillation (ENSO) influences SST predictability in the North Pacific during different phases (El Niño, La Niña, Neutral). Using reanalysis data, this research introduces the concept of predictability limit (PL), revealing an asymmetry in the PL response: La Niña extends the PL to 8.4 months, El Niño shortens it to 5.5 months, and Neutral falls in 5.9 months. This asymmetry aligns with the existing prediction skills. Examining the error growth dynamics, La Niña exhibits a robust SST signal with slower error growth, whereas El Niño displays a weaker signal with faster error growth. Neutral, meanwhile, shows a high signal strength but large error growth. This study sheds light on these differences in SST predictability and provides valuable insights for refining North Pacific SST predictions through model advancements.

1. Introduction

Sea surface temperature (SST) variability in the North Pacific exerts a substantial influence on the weather and climate patterns over the ocean and adjoining continents, notably affecting North America and East Asia (Beattie & Elsberry, 2012; Ding et al., 2015, 2018; Latif & Barnett, 1994; Tao et al., 2019; Zou et al., 2020). This variability, which constitutes a broader aspect known as the Pacific decadal oscillation, has significant implications for global climate variability (Newman et al., 2016; Vijverberg & Coumou, 2022; Wang et al., 2014; Wei et al., 2021). Consequently, a meticulous examination of research and prediction of SST variability in the North Pacific is of paramount importance.

There have been many studies on the prediction and predictability of SST variability in the North Pacific on seasonal to interannual timescales (Comeau et al., 2017; Di Lorenzo et al., 2010; Wen et al., 2012; Zhao et al., 2019). Wen et al. (2012) assessed the skill of North Pacific SST using the National Centers for Environmental Prediction (NCEP) Climate Forecast System (CFS) and demonstrated reasonable prediction skill,

© 2024. The Authors.

This is an open access article under the

terms of the [Creative Commons](https://creativecommons.org/licenses/by/4.0/)

[Attribution-NonCommercial-NoDerivs](https://creativecommons.org/licenses/by/4.0/)

License, which permits use and

distribution in any medium, provided the

original work is properly cited, the use is

non-commercial and no modifications or

adaptations are made.

particularly excluding the Kuroshio-Oyashio Extension (KOE) region, for a two-season lead time, and underscored the influential role of the El Niño-Southern Oscillation (ENSO) in North Pacific SST variability on the seasonal to interannual timescale. Hu et al. (2014) examined SST prediction skill in the North Pacific using a fully coupled forecast system (NCEP CFS version 2), highlighting the impact of the phase relationship between ENSO and North Pacific variability at initial conditions. Zhao et al. (2019) also exhibited high SST prediction skills over most of the North Pacific, particularly when ENSO and North Pacific SST are in phase at initial conditions using the First Institute of Oceanography Earth System Model. Yati and Minobe (2021) corroborated high predictability in the central North Pacific in January linked to ENSO via teleconnection, yet acknowledged limited prediction skills at mid-latitudes. Zhao et al. (2021) separated North Pacific climate variability from tropical dynamics, revealing the significant influence of ENSO on the seasonal evolution of North Pacific SST.

Despite these advancements, coupled climate models still face challenges in predicting North Pacific SST variability. The intricate interactions among multi-scale phenomena give rise to North Pacific SST variability (Newman et al., 2016; Zhao et al., 2021), which introduces challenges to predicting North Pacific SST variability. Newman et al. (2016) succinctly summarized the intricate processes characterizing North Pacific variability as several key components: ocean surface heat fluxes, Ekman transport, ocean memory and re-emergence, decadal changes in the Kuroshio-Oyashio system. Duan and Wu (2014) identified a “summer prediction barrier” in Pacific decadal oscillation-related SST anomalies, emphasizing the challenges in mid-latitude predictions from the perspective of initial error growth in perfect model predictability experiments. The seasonal predictability of SST anomalies in the KOE also exhibited seasonal dependence (Wu & Duan, 2018; Wu et al., 2016). The predictability of North Pacific SST requires further study.

ENSO, acting through the “atmospheric bridge,” plays a pivotal role in the predictability of North Pacific SST variability across seasonal to interannual timescales (Lau & Nath, 2001; Li et al., 2019; Schneider & Cornuelle, 2005; Zhao et al., 2021). Despite recent improvements in prediction skills, particularly in ENSO-affected areas, the influence of different ENSO phases on North Pacific SST predictability remains inadequately quantified (Hu et al., 2014). Moreover, most studies rely on climate models, which introduce limitations (Yati & Minobe, 2021). Recognizing these constraints, the goal of this study is to quantify the predictability limit (PL) of North Pacific variability based on observation/reanalysis data with the nonlinear local Lyapunov exponent (NLLE), compare results under different ENSO phases, and offer a physical explanation grounded in nonlinear error growth dynamics. This research will endeavor to enhance our understanding of Northern Pacific SST variability influenced by ENSO and contribute to the refinement of prediction skills.

2. Methods and Data

2.1. Methods

In this study, we employed the NLLE method, as introduced by Chen et al. (2006) and further elaborated on by Ding and Li (2007), to calculate the PL of the SST in the North Pacific. For a nonlinear dynamical system governed by $\frac{d\mathbf{x}}{dt} = \mathbf{F}(\mathbf{x})$, where \mathbf{x} represents the state vector and $\boldsymbol{\delta} = [\delta_1(t), \delta_2(t), \dots, \delta_n(t)]^T$ denotes the error vector, the NLLE is defined as follows:

$$\lambda(\mathbf{x}(t_0), \boldsymbol{\delta}(t_0), \tau) = \frac{1}{\tau} \ln \frac{\|\boldsymbol{\delta}(t)\|}{\|\boldsymbol{\delta}(t_0)\|}, \quad (1)$$

where $\lambda(\mathbf{x}(t_0), \boldsymbol{\delta}(t_0), \tau)$ is a function of the initial state $\mathbf{x}(t_0)$, the initial error $\boldsymbol{\delta}(t_0)$, and the evolution time of τ , with $\|\cdot\|$ denoting the 2-norm. The NLLE encapsulates the nonlinear growth rate of initial errors within a dynamic system. The ensemble average NLLE, denoted as $\bar{\lambda}(\Omega, \boldsymbol{\delta}, \tau)$, is obtained by averaging the individual NLLE values across a specific class of states Ω :

$$\bar{\lambda}(\Omega, \boldsymbol{\delta}, \tau) = \frac{1}{\tau} \ln \frac{\|\bar{\boldsymbol{\delta}}(t)\|_{\mathbf{x} \in \Omega}}{\|\bar{\boldsymbol{\delta}}(t_0)\|_{\mathbf{x} \in \Omega}}, \quad (2)$$

where $\bar{\mathbf{x}}_{\in \Omega}$ represents the geometric mean of the errors within the state sample set Ω . The ensemble mean NLLE provides insights into the evolution of the mean error growth and serves as a representative measure of predictability for a specific set. The mean relative growth of the initial error (RGIE, \bar{E}) is derived as follows:

$$\ln \bar{E}(\mathbf{x}, \delta, \tau) = [\bar{\lambda}(\Omega, \delta, \tau)\tau] = \ln \frac{\|\delta(t_\tau)\|_{\mathbf{x} \in \Omega}}{\|\delta(t_0)\|_{\mathbf{x} \in \Omega}}. \quad (3)$$

In accordance with dynamical systems error growth theory, $\bar{E}(\mathbf{x}, \delta, \tau)$ converges to a saturation level with increasing τ (Ding & Li, 2007). By utilizing the theoretical saturation level, the PL can be quantitatively determined, as established by Ding and Li (2007) and Li and Ding (2011). A schematic depiction of the PL determination using the NLE method is illustrated in Figure 1 by Ding et al. (2016). For atmospheric and oceanic systems with explicitly unknown dynamical equations, the mean NLE and RGIE can be computed using observational/reanalysis data and the Local Dynamical Analog (LDA) method (Li & Ding, 2011). By identifying analogs in the observational time series using the LDA method, the exponential divergence rate between the base state and its analog is estimated as the NLE, and the mean RGIE is also calculated. The PL is defined as the time at which the relative error reaches 95% of its saturation value. Building on the LDA method proposed by Li and Ding (2011), Hou et al. (2021), and Hou, Li, Wang, et al. (2022) optimized relevant algorithms, introduced the error growth features of persistent forecast, and proposed an improved-LDA method. In this study, we applied the improved-LDA method to identify the analogs. Numerous studies have successfully employed the NLE method to investigate the predictability of atmospheric and oceanic systems (Ding et al., 2008; He et al., 2021; Hou et al., 2018; Hou, Li, Ding, et al., 2022; Li et al., 2018; Mengist & Seo, 2022).

To assess the factors influencing the size of PL, we reformulated Equation 2 as $\tau = \frac{1}{\bar{\lambda}(\Omega, \delta, \tau)} \ln \frac{\|\delta(t_\tau)\|_{\mathbf{x} \in \Omega}}{\|\delta(t_0)\|_{\mathbf{x} \in \Omega}}$. For PL, we obtain:

$$T = \frac{1}{\bar{\lambda}(\Omega, \delta, T)} \ln \frac{\|\delta(t_T)\|_{\mathbf{x} \in \Omega}}{\|\delta(t_0)\|_{\mathbf{x} \in \Omega}}, \quad (4)$$

where T is the PL, $\bar{\lambda}(\Omega, \delta, T)$ represent the error growth rate (namely, NLE) during the evolutionary time of T , and $\frac{\|\delta(t_T)\|_{\mathbf{x} \in \Omega}}{\|\delta(t_0)\|_{\mathbf{x} \in \Omega}}$ is the saturated RGIE. Equation 4 can be further expressed as:

$$\ln T = \ln \left\{ \ln \frac{\|\delta(t_T)\|_{\mathbf{x} \in \Omega}}{\|\delta(t_0)\|_{\mathbf{x} \in \Omega}} \right\} - \ln \bar{\lambda}(\Omega, \delta, T). \quad (5)$$

From Equation 5, the size of the PL is determined by two factors: saturated RGIE and NLE during the evolutionary time T . Thus, the subsequent section elaborates on the distinctions in PL from these dual perspectives.

Bootstrapping, a nonparametric statistical test, was employed in this study. Bootstrapping involves data resampling with replacement to estimate the robustness of nearly any statistic. This statistical approach is particularly advantageous when dealing with small sample sizes, eliminating a priori assumptions regarding the distribution of sample data (Diaconis & Efron, 1983; Hennemuth et al., 2013). Further details regarding bootstrapping are provided in Supporting Information S1.

2.2. Data

The SST data set used in this study was the version 5 of monthly NOAA Extended Reconstructed SST (ERSST.V5) data, which spans a $2^\circ \times 2^\circ$ horizontal grid and encompasses the temporal range from January 1854 to December 2019 (Huang et al., 2017). Supplementary to ERSSTV5, the Hadley Center Sea Ice and SST data set (Rayner et al., 2003) and Merged Hadley-OI SST data set (Hurrell et al., 2008) are employed to corroborate the primary results of this study. Prior to applying the NLE method, climatological mean annual cycles and quadratic trends were removed from the SST data to obtain anomalies. To explain the related physical processes, atmospheric data, including u-wind, v-wind, skin temperature, specific humidity, geopotential height, and surface heat flux, are sourced from the NOAA/CIRES/DOE 20th Century Reanalysis (V3) (Slivinski et al., 2019).

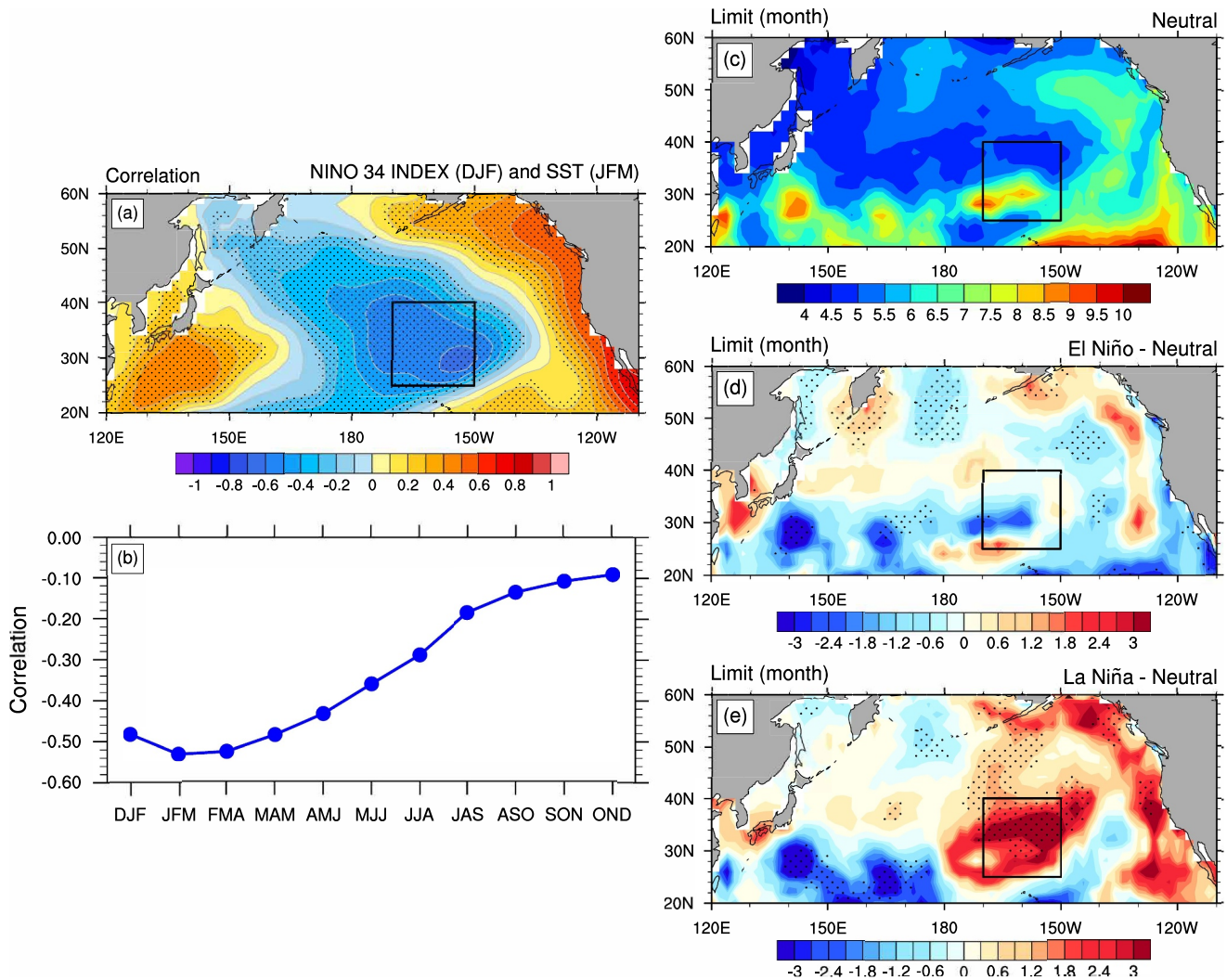


Figure 1. Influence of ENSO on North Pacific sea surface temperature (SST) anomalies and predictability limits: (a) Correlation patterns between the Niño 3.4 index during winter (December, January, February: DJF) and SST in the North Pacific during the subsequent winter months (January, February, March: JFM). (b) Average correlation within the North Pacific box region (25°–40°N, 170°–150°W) between the Niño 3.4 index during DJF and SST in the North Pacific. Seasons for North Pacific SST utilized are represented on the horizontal axis. (c) Predictability limit (unit: month) of SST in the North Pacific from DJF under ENSO Neutral conditions. (d) Discrepancy in the predictability limit (unit: month) of North Pacific SST from DJF between El Niño and Neutral conditions. (e) Similar to (d), but comparing the predictability limit between La Niña and Neutral conditions. The SST data set spans from January 1920 to December 2019, with El Niño, La Niña, and Neutral years detailed in Table S1 and Figure S1 in Supporting Information S1.

3. Predictability Limit of SST in the North Pacific Under Different ENSO Phases

As a coupled air-sea phenomenon primarily manifesting in the tropical Pacific and attaining maturation during winter, ENSO exerts a profound influence on the climate variability of SST in the North Pacific through atmospheric teleconnection (Newman et al., 2016; Zhao et al., 2021). The spatial correlation pattern between the Niño 3.4 index in winter (December, January, February, DJF) and North Pacific SST anomalies in JFM (January, February, March) is illustrated in Figure 1a, revealing a significant negative correlation in the main North Pacific area exceeding -0.4 . This correlation underscores the propensity of warm SST anomalies of ENSO in winter to induce corresponding cold anomalies in the North Pacific, and vice versa. Designing the mean SST anomalies over the region (25°–40°N, 170°–150°W) as the North Pacific Variation (NPV) index, lag correlations between the NPV index and the Niño 3.4 index (DJF) are depicted in Figure 1b. The peak correlation occurs between Niño 3.4 index (DJF) and NPV index (JFM) with a 1-month lag, which is aligned with the findings of Newman et al. (2016) and confirms the enduring influence of winter ENSO on SST evolution in the North Pacific through JAS (July, August, September). Despite the evident influence of ENSO on the North Pacific, the distinct phases of

ENSO—neutral, cold (La Niña), and warm (El Niño)—prompted an inquiry into their respective effects on SST predictability in the region. To address this, El Niño events were identified as those with Niño 3.4 index in DJF exceeding 1°C, La Niña events as those with an index lower than −1°C, and Neutral events encompassed years with an index between −0.5°C and 0.5°C from DJF to JJA (June, July, August). The classification results, summarized in Table S1 in Supporting Information S1 and illustrated in Figure S1 in Supporting Information S1, yielded 16 El Niño, 17 La Niña, and 17 Neutral events.

Figures 1c–1e present the PL patterns of the North Pacific under ENSO-neutral phases and the disparities between ENSO warm/cold and neutral phases. The complete PL results under different ENSO phases and their differences are depicted in Figure S2 in Supporting Information S1. Spatial disparities in PL are discernible, with higher PL in the eastern North Pacific than in its western counterpart. Specifically, the PL in the eastern North Pacific surpasses 6.5 months in Neutral years, whereas the western North Pacific registers a PL of only 5 months. This spatial contrast in PL is attributed to the influence of ocean mesoscale activity, particularly notable in the KOE region. Notably, differences in PL emerge based on distinct ENSO phases. La Niña exhibits higher PL than El Niño and Neutral conditions, extending to both the NPV region and the eastern North Pacific (Figure 1e; Figures S2e and S2f in Supporting Information S1). The disparities in PL between La Niña and Neutral phases reach 2.4 months in the NPV region, surpassing a 90% confidence level. In contrast, El Niño conditions yield lower PL in the southern North Pacific, albeit with marginal differences (Figure 1d). In the NPV region, the mean PL under El Niño is 5.5 months, under La Niña is 8.4 months, and under Neutral is 5.9 months (Figure 3a). The differences in PL between El Niño and Neutral conditions are not significant in the NPV region, emphasizing the asymmetric effects of warm and cold ENSO phases on the North Pacific.

The observed higher PL during La Niña phases and lower PL during El Niño phases, compared with Neutral conditions, are substantiated by model forecast skill from the North American Multi-Model Ensemble (NMME). Examining the period from January 1982 to December 2010, the correlation skill of La Niña was the highest, whereas that of El Niño was the lowest at almost all lead times from 0 to 8 months (Figure S3 in Supporting Information S1), aligned with the PL features.

4. Error Growth Characteristics and Physical Processes Under Different ENSO Phases

As expressed by Equation 5, the PL is intricately linked to the saturation relative error (saturated RGIE) and error growth rate (NLLE) at the saturation time. Figures 2a and 2b show the calculated NLLE and RGIE ($\ln \bar{E}$) for the NPV region across different ENSO phases. The NLLE signifies the relative error growth rate during the different stages of evolution. As depicted in Figure 2a, the NLLE during La Niña is comparable to that during Neutral conditions but exceeds that during El Niño in the evolutionary time of 1–2 months. With increasing evolution time, the NLLE during La Niña becomes lower than that under both Neutral and El Niño conditions in the evolutionary time of 4–7 months, contributing to the heightened PL during La Niña compared to Neutral conditions. Furthermore, the RGIE under diverse ENSO phases gradually increases and eventually saturates as the evolution progresses (Figure 2b). The absolute error curves in Figure 2c reveal that, in the later stages of evolution (6–10 months), the absolute error under La Niña is the smallest, whereas under El Niño and Neutral conditions, the errors are nearly equivalent, aligning with the asymmetric characteristics of PL among the three ENSO phases. As a direct depiction of the PL from Figure 2b, Figure 3a illustrates the PL and its corresponding uncertainty ranges in the NPV region under different ENSO phases, which are consistent with the findings in Figures 1c–1e, where the PL under La Niña is significantly higher than that under El Niño and Neutral conditions. The PL under Neutral conditions is higher than that under El Niño conditions, although the PL difference is not significant.

Examination of the saturated RGIE in Figure 3b reveals intriguing dynamics. Under El Niño conditions, the saturated RGIE, as the prediction signal intensity, is notably diminished compared to its La Niña and Neutral counterparts, which is consistent with the minimum PL under El Niño conditions. However, the saturated RGIE in Neutral conditions closely mirrors that of La Niña, contrary to the observed divergence in the PL between El Niño and Neutral conditions. Notably, the NLLE under Neutral conditions surpasses that in both the El Niño and La Niña phases throughout the evolutionary timeframe of 1–8 months, as shown in Figure 2a. The rapid growth of RGIE under Neutral conditions during the evolutionary time from 3 to 6 months is also evident in Figure 2b. Considering Equation 5, Figure 3c shows the NLLE in PL(T), indicating a significantly higher NLLE(T) under El Niño and Neutral conditions compared to that of La Niña, whereas the NLLE(T) under El Niño is not significantly

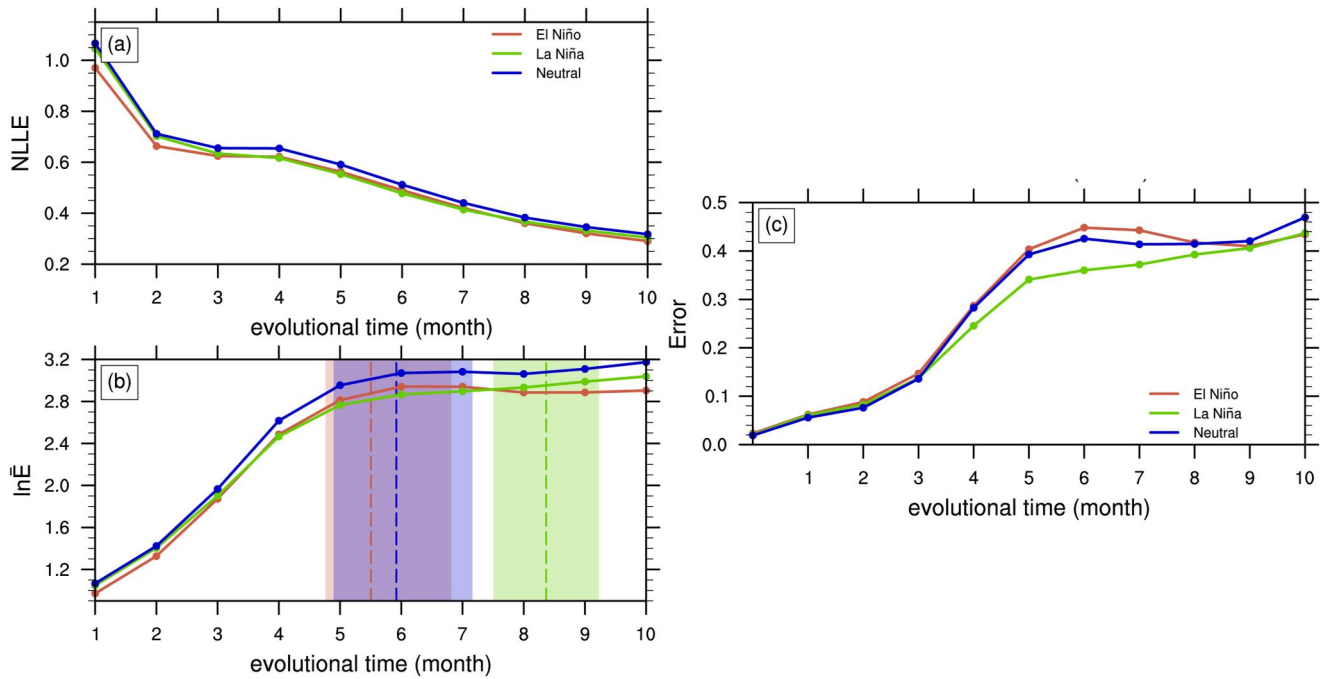


Figure 2. Error growth dynamics in the focused North Pacific region (25° – 40° N, 170° – 150° W) under El Niño (red), La Niña (green), and Neutral (blue) conditions: (a) Assessment of error growth rate, quantified by the nonlinear local Lyapunov exponent (NLLE). (b) Relative error to initial error (RGIE) across different evolutionary time periods. The dashed line is the predictability limit, whereas the shaded area signifies the associated uncertainty range (10%–90%). (c) Absolute error over varying time intervals.

different from that under Neutral conditions. It is imperative to acknowledge the temporal distinctions in PL(T) under diverse ENSO phases, which complicate the interpretation of the NLLE. Considering that PL(T) under different ENSO phases is approximately 6 months, Figure 3d displays the NLLE during a 6-month evolutionary time. Evidently, NLLE(6) mirrors the characteristics of NLLE(T); it is the smallest under La Niña conditions, with no significant difference between El Niño and Neutral conditions. Hence, the size of NLLE(6) influences the PL, underscoring the role of NLLE(T). The 6-month evolution period is subjectively segmented into early (0–3 months) and late (3–6 months) stages. Figures 3e and 3f show the relative growth of errors in the two periods, shedding light on the period of error growth that exerts the greater impact. During the early evolutionary period (0–3 months), the RGIE(0–3) under Neutral conditions is the highest, followed by La Niña, whereas El Niño corresponds to the smallest conditions. In the evolutionary period of 3–6 months, the RGIE under La Niña is the smallest, with the RGIE under El Niño and Neutral conditions being nearly equivalent. These patterns align with the characteristics of the three types of events depicted in NLLE(T) and NLLE(6), indicating that error growth over 3–6 months plays a decisive role in determining the error growth rate (NLLE) over the entire period, consequently impacting PL size.

In summary, the elevated PL during La Niña can be attributed to a substantially saturated RGIE and a low error growth rate (NLLE(T)). For El Niño, the saturated RGIE is smaller, and the error growth rate is relatively larger than under those La Niña and Neutral conditions. Under Neutral conditions, the saturated RGIE is relatively larger, but the error growth rate is smaller than that under La Niña conditions. These features ultimately result in a smaller PL under El Niño and Neutral conditions than under La Niña conditions. The disparity in the error growth rate (NLLE) primarily stems from the error growth features in the evolution time of 3–6 months. Further exploration is warranted to discern the factors influencing the saturated RGIE and relative error growth (RGIE) during 3–6 months in the three ENSO phases.

To elucidate the saturated RGIE, we consider the amplitude of SST anomalies in the later evolutionary period. The larger the amplitude, represented by a 2-norm, the stronger the predicted signal. Given the inherent disparity in the initial SST anomalies across different ENSO phases, we employ a signal-to-noise ratio approach for a more objective assessment. This involves using the variance of the square of the initial SST anomaly as noise and the

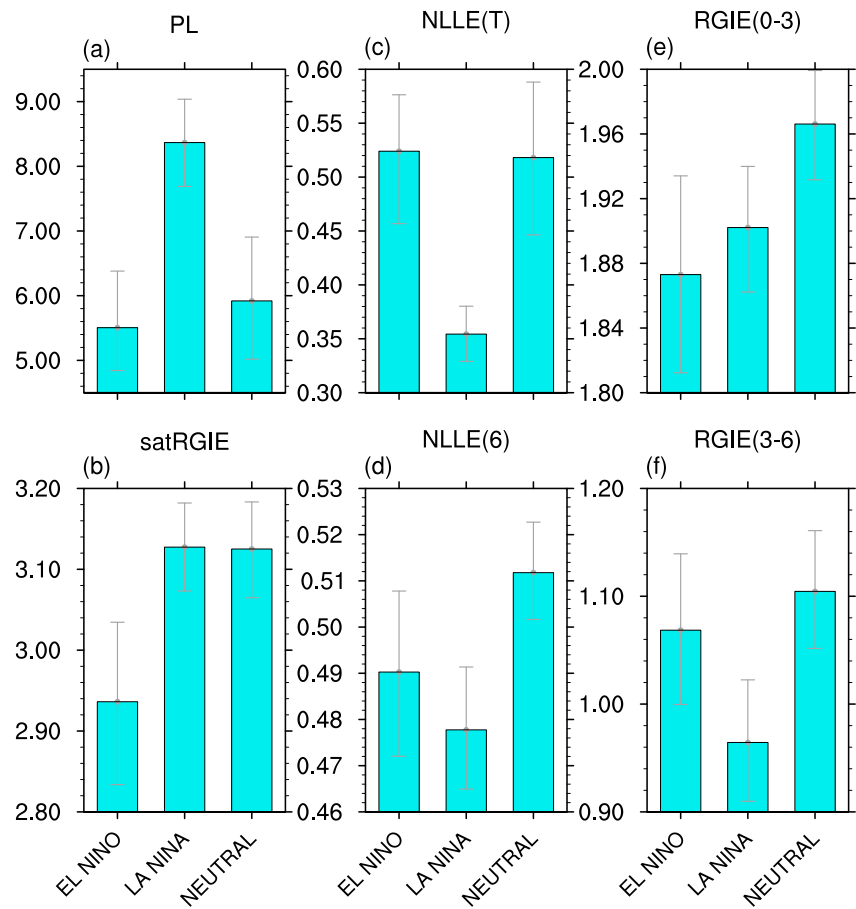


Figure 3. Predictability limits and error growth dynamics in the focused North Pacific region (25°–40°N, 170°–150°W) under different ENSO conditions: (a) Predictability limit, (b) saturation relative growth to initial error (RGIE), (c) error growth rate (NLLE) at saturation time, (d) NLLE at 6-month time, (e) RGIE during the evolutionary period of 0–3 months, and (f) RGIE during the evolutionary period of 3–6-month time. The abscissa denotes different ENSO conditions. Error bars represent the range values from 10% to 90%.

variance of the SST anomalies in later evolutionary stages as signal information. Following the signal-to-noise ratio concept, we define the signal ratio as $\ln \frac{(SSTa(6-12))^2}{(SSTa(0))^2}$, where SSTa(6–12) represents the SST anomaly in the evolutionary time of 6–12 months, and SSTa(0) is the SST anomaly in the evolutionary time of 0 month. Figure 4a illustrates the signal ratio, revealing that it is smallest under El Niño conditions, with almost equivalent values under La Niña and Neutral conditions. This correspondence aligns with the magnitude of the saturated RGIE, indicating that the magnitude of SST anomalies in the North Pacific significantly influences forecast signals, thereby contributing to the observed differences in PL under distinct ENSO phases.

By examining the physical mechanisms governing error growth rates during the evolutionary period of 3–6 months, we considered that the atmosphere, acting as an external force, introduces noise, thereby increasing the complexity and chaos of the system (Kumar & Zhu, 2018). Thus, the elevated uncertainty in SST anomalies forced by atmospheric evolution leads to a heightened error growth rate, increased prediction difficulty, and reduced PL. Thermal forcing is the principal driver of this atmospheric influence on SST. Figure 4b shows the anomalous effect of atmospheric heat flux on the ocean. Under La Niña conditions, an anomaly in the net heat flux from the ocean to the atmosphere has been observed. Conversely, during the El Niño and Neutral phases, the net heat flux imparts heat to the ocean from the atmosphere during the evolutionary period from 3 to 6 months. This distinction implies that, in the case of La Niña, the ocean exerts a more significant influence on the atmosphere, thereby minimizing noise effects. Consequently, the error growth rate is the smallest during La Niña, whereas the El Niño and Neutral phases experience comparatively larger error growth rates.

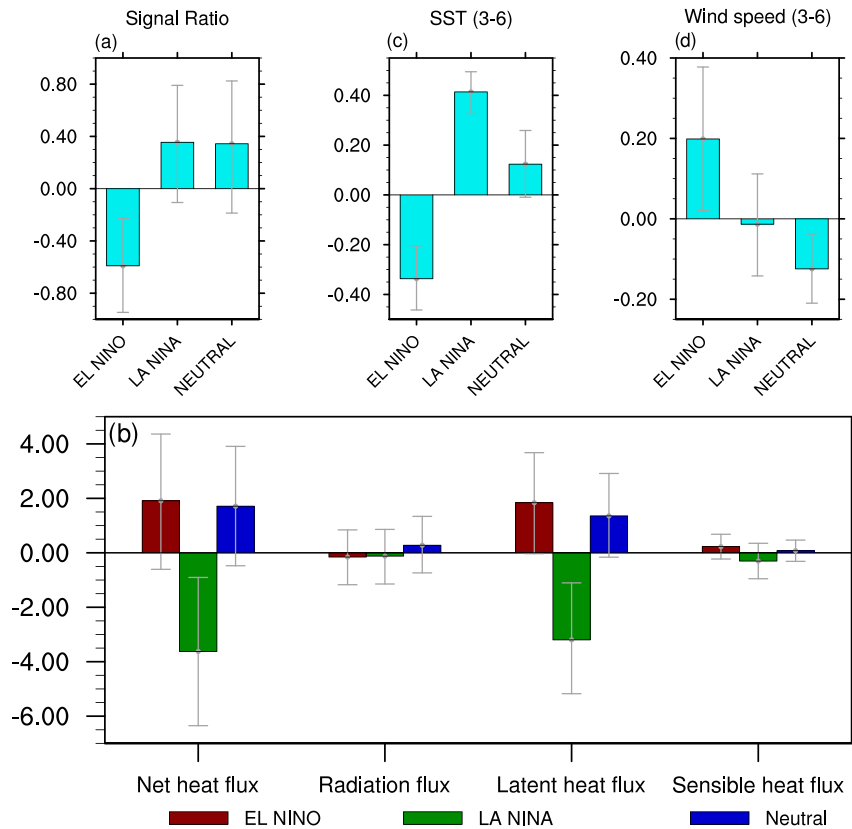


Figure 4. Investigation of ocean-atmosphere interaction features in the focused North Pacific region (25° – 40° N, 170° – 150° W) under distinct ENSO conditions: (a) Signal ratio represented by $\ln \frac{(SSTa(6-12))^2}{(SSTa(0))^2}$. (b) Anomalies in heat flux (net heat flux, radiation flux, latent heat flux, sensible heat flux) under various ENSO conditions (color bars) during the evolutionary period of 3–6 months. (c) Sea surface temperature anomalies. (d) Wind speed anomalies averaged over the time interval from 3 to 6 months. The abscissa of (a, c, and d) denotes different ENSO conditions. Positive values in (b) signify heat transfer from the atmosphere to the ocean. Error bars indicate a value range of 10%–90%.

Considering the components of the surface heat flux, including the radiation net flux, latent heat net flux, and sensible net heat flux, Figure 4b provides a detailed presentation. The latent heat flux, which is influenced by SST anomalies and wind speed, plays a pivotal role in determining the overall features of the net heat flux. We illustrate the scenarios of SST anomalies under different ENSO phases and wind speeds during the evolutionary period of 3–6 months in Figures 4c and 4d. Under La Niña conditions, the SST anomaly in the North Pacific-focused region is notably larger (Figure 4c), fostering increased heat transfer to the atmosphere. In the El Niño scenario, relatively cold SST anomalies facilitate heat transfer from the atmosphere to the ocean, thereby introducing noise. This SST discrepancy is a consequence of atmospheric anomalies induced by ENSO. As depicted in Figure S4 in Supporting Information S1, during the El Niño influence, the SST anomaly in the North Pacific region portrays a negative state persisting until April to June (evolution time of 4–6 months). Simultaneously, this period is characterized by negative specific humidity, which hinders latent transfer from the ocean to the atmosphere. In the La Niña scenario, the SST anomaly in the North Pacific demonstrates a positive state, corresponding to a positive specific humidity condition that facilitates the transfer of latent heat from the ocean to the atmosphere. Under Neutral conditions, the SST anomaly in the North Pacific region is weakly positive, accompanied by a mildly positive specific humidity anomaly. Consequently, the latent heat transfer from the ocean to the atmosphere under Neutral conditions is weaker than that under La Niña conditions but higher than that under El Niño conditions (Figure 4b).

According to the empirical formula for latent heat, the magnitude of wind speed also exerts an influence. As shown in Figure 4d, during the evolution time of 3–6 months, the wind speed under El Niño conditions is unusually high, whereas under Neutral conditions, it exhibits a negative wind speed anomaly. However, the wind

speed anomalies in all three cases are relatively small. As illustrated in Figure S5 in Supporting Information S1, distinct ENSO phases induce geopotential height anomalies in the North Pacific region during winter through atmospheric bridges. Specifically, under El Niño conditions, the Aleutian low strengthens, leading to heightened wind speeds and favorable evaporation and cooling, resulting in negative SST anomalies (Figure S4a in Supporting Information S1). In the case of La Niña, the Aleutian low weakens, causing a reduction in wind speed. A positive SST anomaly (Figure S4b in Supporting Information S1) ensues through the wind-evaporation-SST mechanism. In the Neutral case, the wind speed weakens, albeit with a small intensity anomaly, corresponding to a weak positive SST anomaly (Figure S4c in Supporting Information S1) and reduces turbulence; thus, the latent heat is transported from the ocean to the atmosphere (Figure 4b). Over time, both atmospheric geopotential height anomalies and wind speed anomalies display less persistence than SST. During the evolutionary period of 3–6 months, the wind speed anomaly is notably weak, as depicted in Figure 4d. The characteristics of the wind speed distribution do not align with the latent heat anomalies. In summary, winter ENSO predominantly influences SST in the North Pacific through the atmospheric bridge, and the SST anomaly persists, resulting in latent heat anomalies over an evolutionary period of 3–6 months, thereby contributing to variations in net heating anomalies across different ENSO phases. Ultimately, the intensity of the noise input from the atmosphere to the ocean varies, leading to differences in error growth under distinct ENSO phases.

5. Conclusions and Discussions

The North Pacific SST variability significantly influences global climate. ENSO plays a direct role in shaping North Pacific SST through the atmospheric bridge; however, its specific impact on predictability remains elusive. This study employed reanalysis data spanning over a century, irrespective of model limitations, to quantitatively assess the PL in North Pacific SST under different ENSO phases, utilizing the NLE method from the perspective of error growth dynamics.

The results revealed discernible differences in the PL of the NPV following distinct winter ENSO phases. Specifically, the PL of the NPV under La Niña (8.4 months) is longer than that under Neutral (5.9 months) and El Niño (5.5 months) conditions. The impacts of La Niña and El Niño on the PL of the NPV manifest asymmetrically. From the error growth dynamics perspective, in comparison to the results under the La Niña phase, the saturated RGIE is smaller under El Niño, and its error growth rate is faster, particularly during the 3–6-month period (April, May, June), leading to a diminished PL under El Niño conditions. Physically, the magnitude of the saturated RGIE correlates with the strength of the SST anomalies in the later stages of evolution, whereas the difference in the error growth rate is attributed to atmospheric noise forcing. Winter ENSO phases induce abnormal SST in the North Pacific, which persists for 3–6 months. La Niña induces significant warm North Pacific SST anomalies, whereas El Niño and neutral phases exhibit negative or nonsignificant NPV anomalies. Warm SST anomalies facilitate ocean-atmosphere heat exchange, reducing the transmission of atmospheric noise to the ocean and resulting in a higher PL under La Niña conditions.

This study compared the influence of different ENSO phases on the predictability of North Pacific SST using reanalysis data sets with the composition method. However, owing to data sample limitations, the estimated PL may be smaller than the true values (Li & Ding, 2011). Furthermore, the composition method does not provide a quantitative result of the ENSO's impact on North Pacific SST predictability. In future research, historical simulation data from WCRP Coupled Model Intercomparison Project could be employed to validate results and quantify the contribution of ENSO to the predictability of North Pacific SST by utilizing the conditional NLE method (Li & Ding, 2015). In addition, the effect of ENSO on the predictability of the North Pacific Ocean through oceanic processes deserves further study.

Data Availability Statement

The sea surface temperature can be found at <https://psl.noaa.gov/data/gridded/data.noaa.ersst.v5.html>, <https://www.metoffice.gov.uk/hadobs/hadisst/>, https://gdex.ucar.edu/dataset/158_asphilli.html. NOAA/CIRES/DOE 20th Century Reanalysis (V3) data is available at https://psl.noaa.gov/data/gridded/data.20thC_ReanV3.html. The North American Multi-Model Ensemble (NMME) data set was downloaded from <https://iridl.ldeo.columbia.edu/SOURCES/Models/.NMME/>.

Acknowledgments

This work was jointly sponsored by the National Natural Science Foundation of China (NSFC) Project (42130607, 42005049), Laoshan Laboratory (No. LSKJ202202600), the Shandong Natural Science Foundation Project (ZR2019ZD12 and ZR2020QD056), and NSFC (42075025, 42105054). We thank the two anonymous reviewers and Drs. Zheng Chen, Yishuai Jin, Yuwei Wang for their assistance in improving our manuscript.

References

- Beattie, J. C., & Elsberry, R. L. (2012). Western North Pacific monsoon depression formation. *Weather and Forecasting*, 27(6), 1413–1432. <https://doi.org/10.1175/WAF-D-11-00094.1>
- Chen, B., Li, J., & Ding, R. (2006). Nonlinear local Lyapunov exponent and atmospheric predictability research. *Science in China - Series D: Earth Sciences*, 49(10), 1111–1120. <https://doi.org/10.1007/s11430-006-1111-0>
- Comeau, D., Zhao, Z., Giannakis, D., & Majda, A. J. (2017). Data-driven prediction strategies for low-frequency patterns of North Pacific climate variability. *Climate Dynamics*, 48(5), 1855–1872. <https://doi.org/10.1007/s00382-016-3177-5>
- Diaconis, P., & Efron, B. (1983). Computer-intensive methods in statistics. *Scientific American*, 248(5), 116–131. <https://doi.org/10.1038/scientificamerican0583-116>
- Di Lorenzo, E., Cobb, K. M., Furtado, J. C., Schneider, N., Anderson, B. T., Bracco, A., et al. (2010). Central Pacific El Niño and decadal climate change in the North Pacific Ocean. *Nature Geoscience*, 3(11), 762–765. <https://doi.org/10.1038/ngeo984>
- Ding, R., & Li, J. (2007). Nonlinear finite-time Lyapunov exponent and predictability. *Physics Letters A*, 364(5), 396–400. <https://doi.org/10.1016/j.physleta.2006.11.094>
- Ding, R., Li, J., & Ha, K. J. (2008). Trends and interdecadal changes of weather predictability during 1950s–1990s. *Journal of Geophysical Research*, 113(24), 1–11. <https://doi.org/10.1029/2008JD010404>
- Ding, R., Li, J., Tseng, Y., Li, L., Sun, C., & Xie, F. (2018). Influences of the North Pacific Victoria mode on the South China sea summer monsoon. *Atmosphere*, 9(6), 229. <https://doi.org/10.3390/atmos9060229>
- Ding, R., Li, J., Tseng, Y. H., Sun, C., & Guo, Y. (2015). The victoria mode in the North Pacific linking extratropical sea level pressure variations to ENSO. *Journal of Geophysical Research*, 120(1), 27–45. <https://doi.org/10.1002/2014JD022221>
- Ding, R., Li, J., Zheng, F., Feng, J., & Liu, D. (2016). Estimating the limit of decadal-scale climate predictability using observational data. *Climate Dynamics*, 46(5–6), 1563–1580. <https://doi.org/10.1007/s00382-015-2662-6>
- Duan, W., & Wu, Y. (2014). Season-dependent predictability and error growth dynamics of Pacific Decadal Oscillation-related sea surface temperature anomalies. *Climate Dynamics*, 44(3–4), 1053–1072. <https://doi.org/10.1007/s00382-014-2364-5>
- He, W., Xie, X., Mei, Y., Wan, S., & Zhao, S. (2021). Decreasing predictability as a precursor indicator for abrupt climate change. *Climate Dynamics*, 56(11), 3899–3908. <https://doi.org/10.1007/s00382-021-05676-1>
- Hennemuth, B., Bender, S., Buelow, K., Dreier, N., Keup-Thiel, E., Krueger, O., et al. (2013). Statistical methods for the analysis of simulated and observed climate data, applied in projects and institutions dealing with climate change impact and adaptation (p. 135). S.
- Hou, Z., Li, J., Ding, R., & Feng, J. (2022). Investigating decadal variations of the seasonal predictability limit of sea surface temperature in the tropical Pacific. *Climate Dynamics*, 59(3–4), 1079–1096. <https://doi.org/10.1007/s00382-022-06179-3>
- Hou, Z., Li, J., Ding, R., Karamperidou, C., Duan, W., Liu, T., & Feng, J. (2018). Asymmetry of the predictability limit of the warm ENSO phase. *Geophysical Research Letters*, 45(15), 7646–7653. <https://doi.org/10.1029/2018GL077880>
- Hou, Z., Li, J., Wang, L., Zhang, Y., & Liu, T. (2022). Improving the forecast accuracy of ECMWF 2-m air temperature using a historical dataset. *Atmospheric Research*, 273, 106177. <https://doi.org/10.1016/j.atmosres.2022.106177>
- Hou, Z., Li, J., & Zuo, B. (2021). Correction of monthly SST forecast in CFSv2 using the local dynamical analog method. *Weather and Forecasting*, 30(4), 843–858. <https://doi.org/10.1175/waf-d-20-0123.1>
- Hu, Z. Z., Kumar, A., Huang, B., Zhu, J., & Guan, Y. (2014). Prediction skill of north pacific variability in NCEP climate forecast system version 2: Impact of ENSO and beyond. *Journal of Climate*, 27(11), 4263–4272. <https://doi.org/10.1175/JCLI-D-13-00633.1>
- Huang, B., Thorne, P. W., Banzon, V. F., Boyer, T., Chepurin, G., Lawrimore, J. H., et al. (2017). Extended reconstructed sea surface temperature, version 5 (ERSSTv5): Upgrades, validations, and intercomparisons. *Journal of Climate*, 30(20), 8179–8205. <https://doi.org/10.1175/JCLI-D-16-0836.1>
- Hurrell, J. W., Hack, J. J., Shea, D., Caron, J. M., & Rosinski, J. (2008). A new sea surface temperature and sea ice boundary dataset for the community atmosphere model. *Journal of Climate*, 21(19), 5145–5153. <https://doi.org/10.1175/2008JCLI2292.1>
- Kumar, A., & Zhu, J. (2018). Spatial variability in seasonal prediction skill of SSTs: Inherent predictability or forecast errors? *Journal of Climate*, 31(2), 613–621. <https://doi.org/10.1175/JCLI-D-17-0279.1>
- Latif, M., & Barnett, T. P. (1994). Causes of decadal climate variability over the North Pacific and North America. *Science*, 266(5185), 634–637. <https://doi.org/10.1126/science.266.5185.634>
- Lau, N.-C., & Nath, M. J. (2001). Impact of ENSO on SST variability in the North Pacific and North Atlantic: Seasonal dependence and role of extratropical sea–air coupling. *Journal of Climate*, 14(13), 2846–2866. [https://doi.org/10.1175/1520-0442\(2001\)014<2846:IOEOSV>2.0.CO;2](https://doi.org/10.1175/1520-0442(2001)014<2846:IOEOSV>2.0.CO;2)
- Li, J., & Ding, R. (2011). Temporal–spatial distribution of atmospheric predictability limit by local dynamical analogs. *Monthly Weather Review*, 139(10), 3265–3283. <https://doi.org/10.1175/MWR-D-10-05020.1>
- Li, J., & Ding, R. Q. (2015). Weather forecasting: Seasonal and interannual weather prediction. In *Encyclopedia of atmospheric sciences* (2nd ed., Vol. 6, pp. 303–312).
- Li, J., Feng, J., & Ding, R. (2018). Attractor radius and global attractor radius and their application to the quantification of predictability limits. *Climate Dynamics*, 51(5–6), 2359–2374. <https://doi.org/10.1007/s00382-017-4017-y>
- Li, J., Zheng, F., Sun, C., Feng, J., & Wang, J. (2019). Pathways of influence of the Northern Hemisphere mid-high latitudes on East Asian climate: A review. *Advances in Atmospheric Sciences*, 36(9), 902–921. <https://doi.org/10.1007/s00376-019-8236-5>
- Mengist, C. K., & Seo, K. (2022). How long can the MJO be predicted during the combined phases of ENSO and QBO? *Geophysical Research Letters*, 49(8), e2022GL097752. <https://doi.org/10.1029/2022GL097752>
- Newman, M., Alexander, M. A., Ault, T. R., Cobb, K. M., Deser, C., Di Lorenzo, E., et al. (2016). The Pacific decadal oscillation, revisited. *Journal of Climate*, 29(12), 4399–4427. <https://doi.org/10.1175/JCLI-D-15-0508.1>
- Rayner, N. A., Parker, D. E., Horton, E. B., Folland, C. K., Alexander, L. V., Rowell, D. P., et al. (2003). Global analyses of sea surface temperature, sea ice, and night marine air temperature since the late nineteenth century. *Journal of Geophysical Research*, 108(D14), 4407. <https://doi.org/10.1029/2002JD002670>
- Schneider, N., & Cornuelle, B. D. (2005). The forcing of the Pacific decadal oscillation. *Journal of Climate*, 18(21), 4355–4373. <https://doi.org/10.1175/JCLI3527.1>
- Slivinski, L. C., Compo, G. P., Whitaker, J. S., Sardeshmukh, P. D., Giese, B. S., McColl, C., et al. (2019). Towards a more reliable historical reanalysis: Improvements for version 3 of the Twentieth Century Reanalysis system. *Quarterly Journal of the Royal Meteorological Society*, 145(724), 2876–2908. <https://doi.org/10.1002/qj.3598>
- Tao, L., Sun, X., & Yang, X.-Q. (2019). The asymmetric atmospheric response to the midlatitude North Pacific SST anomalies. *Journal of Geophysical Research: Atmospheres*, 124(16), 9222–9240. <https://doi.org/10.1029/2019JD030500>

- Vijverberg, S., & Coumou, D. (2022). The role of the Pacific Decadal Oscillation and ocean-atmosphere interactions in driving US temperature predictability. *Npj Climate and Atmospheric Science*, 5(1), 1–11. <https://doi.org/10.1038/s41612-022-00237-7>
- Wang, S., Huang, J., He, Y., & Guan, Y. (2014). Combined effects of the Pacific decadal oscillation and El Niño-Southern Oscillation on global land dry–wet changes. *Scientific Reports*, 4(1), 6651. <https://doi.org/10.1038/srep06651>
- Wei, W., Yan, Z., & Li, Z. (2021). Influence of Pacific decadal oscillation on global precipitation extremes. *Environmental Research Letters*, 16(4), 044031. <https://doi.org/10.1088/1748-9326/abed7c>
- Wen, C., Xue, Y., & Kumar, A. (2012). Seasonal prediction of north pacific SSTs and PDO in the NCEP CFS hindcasts. *Journal of Climate*, 25(17), 5689–5710. <https://doi.org/10.1175/JCLI-D-11-00556.1>
- Wu, Y., & Duan, W. (2018). Impact of SST anomaly events over the Kuroshio–Oyashio Extension on the “summer prediction barrier.”. *Advances in Atmospheric Sciences*, 35(4), 397–409. <https://doi.org/10.1007/s00376-017-6322-0>
- Wu, Y., Duan, W., & Rong, X. (2016). Seasonal predictability of sea surface temperature anomalies over the Kuroshio–Oyashio Extension: Low in summer and high in winter. *Journal of Geophysical Research: Oceans*, 121(9), 6862–6873. <https://doi.org/10.1002/2016JC011887>
- Yati, E., & Minobe, S. (2021). Sea surface temperature predictability in the North Pacific from multi-model seasonal forecast. *Journal of Oceanography*, 77(6), 897–906. <https://doi.org/10.1007/s10872-021-00618-1>
- Zhao, Y., Newman, M., Capotondi, A., Di Lorenzo, E., & Sun, D. (2021). Removing the effects of tropical dynamics from North Pacific climate variability. *Journal of Climate*, 1–49. <https://doi.org/10.1175/JCLI-D-21-0344.1>
- Zhao, Y., Yin, X., Song, Y., & Qiao, F. (2019). Seasonal prediction skills of FIO-ESM for North Pacific sea surface temperature and precipitation. *Acta Oceanologica Sinica*, 38(1), 5–12. <https://doi.org/10.1007/s13131-019-1366-x>
- Zou, Q., Ding, R., Li, J., Tseng, Y., Hou, Z., Wen, T., & Ji, K. (2020). Is the North Pacific Victoria mode a predictor of winter rainfall over South China? *Journal of Climate*, 33(20), 8833–8847. <https://doi.org/10.1175/JCLI-D-19-0789.1>